Supporting Information

Harnessing Slow Photons in 3D Silica Photonic Crystals for Efficient and Catalyst-Free Removal of Chromophoric Organic Pollutants

Tharishinny Raja Mogan*[a], Ruo Qi Ho[a], Veronica Pereira[a], Carice Chong[a], Siew Kheng Boong[a], Eugene Yee Shuen Chua[a], Hiang Kwee Lee*[a,b]

Affiliations:

[a] Division of Chemistry and Biological Chemistry, School of Chemistry, Chemical Engineering and Biotechnology, Nanyang Technological University, 21 Nanyang Link, Singapore 637371, Singapore.

[b] Institute of Materials Research and Engineering, The Agency for Science, Technology and Research (A∗STAR), 2 Fusionopolis Way, #08-03, Innovis, 138634, Singapore.

*Corresponding author: tharishinny.rm@ntu.edu.sg, hiangkwee@ntu.edu.sg

Experimental Section

Chemicals

Styrene (C_8H_8, ≥99%), potassium persulfate ($K_2S_2O_8$, ≥99%), poly(sodium 4-styrenesulfonate) ($C_8H_7SO_3Na$, average MW ~70000), potassium bicarbonate ($KHCO_3$, ACS reagent), tetraethyl orthosilicate (TEOS, 98%, reagent grade), ammonium hydroxide solution (28.0-30.0%, NH_3 basis, ACS grade), methylene blue, malachite green oxalate, rhodamine 6G (ACS reagent), and concentrated HCl (37%) were purchased from Sigma-Aldrich. Ethanol (≥98%, AR grade) was obtained from Fischer Chemical. Argon (Ar; 99.9995%) was purchased from Leeden National Oxygen Ltd. All chemicals were used without further purification. Milli-Q water (> 18.0 MΩ.cm) was purified with a Sartorius Arium 611® UV ultrapure water system.

Synthesis of polystyrene (PS) nanospheres

The polystyrene spheres were synthesized via emulsion polymerization.[1] A pre-defined amount of potassium bicarbonate and poly(sodium 4-styrenesulfonate) was first dissolved in 100 mL ultrapure water under continuous stirring at 500 rpm. Once fully dissolved, the solution was transferred to a 300 mL three-necked round-bottom flask. Argon gas was purged through the solution for 20 minutes to remove dissolved oxygen. Subsequently, 13 mL styrene monomer was added, and the mixture was stirred at 900 rpm under an argon environment. The solution was then heated to 72°C, after which 25 mL of a pre-heated potassium persulfate solution (0.25 g) was added dropwise over 14 minutes. The system was sealed and maintained at 72 °C with continuous stirring (900 rpm) for 24 hours. The resulting colloidal suspension was centrifuged at 8000 rpm for 15 minutes to collect the polystyrene nanospheres, which were subsequently washed with ample amount of water and ethanol, and dried under vacuum. Polystyrene spheres with diameters of 302 nm, 397 nm, and 479 nm were obtained by varying the concentrations of potassium bicarbonate and poly (sodium 4-styrenesulfonate), while all other parameters remained constant.

Fabrication of polystyrene opal

Polystyrene (PS) opals were fabricated via a self-assembly process assisted by centrifugation.[2] A 1 wt% dispersion of PS spheres in ethanol was first sonicated for 10 minutes to ensure uniform particle dispersion. The suspension was then centrifuged at 2000 rpm for approximately 20 minutes. After centrifugation, the clear supernatant was carefully decanted,

and the remaining sediment was dried under vacuum. The resulting sediment was further dried in an oven at 80 °C for 1 hour, yielding three-dimensionally ordered PS opal structures.

Preparation of SiO_2 inverse opal

Silica inverse opals were fabricated by infiltrating PS opal templates with a sol-gel silica precursor, followed by thermal removal of the PS template via calcination. The precursor solution was prepared by mixing 3 mL TEOS, 2 mL ethanol, 1.5 mL deionized water, and 0.5 mL concentrated HCl under continuous stirring for 1 hour. Infiltration was performed by adding the diluted silica precursor solution (1:4 v/v in ethanol) to a centrifuge tube containing dried PS opal powder, ensuring complete coverage of the surface. Vacuum-assisted infiltration was carried out for 15 minutes to fill the interstitial voids of the colloidal crystal. Excess precursor was carefully removed using filter paper to minimize gelation. This infiltration and removal process was repeated for two cycles. The infiltrated samples were then dried under vacuum. To remove the PS template, the samples underwent calcination in air, with the temperature ramped from room temperature to 500 °C at a rate of 3 °C/min, held at 500 °C for 2 hours, and then cooled gradually to room temperature. Silica inverse opals with pore diameters of 242 nm, 343 nm, and 400 nm were obtained, corresponding to the original PS sphere sizes.

Fabrication of SiO_2 nanoparticles

SiO_2 nanoparticles were synthesized using a modified Stober method.[3] Briefly, 37.61 mL of ethanol, 6.75 mL of ultrapure water, and 1.2 mL of ammonium hydroxide solution were added to a conical flask and stirred at 500 rpm for 15 minutes. TEOS was then added dropwise to the ethanolic solution in volume of 3.35 mL to produce SiO_2 nanoparticles with diameter of 325 nm. The mixture was stirred at room temperature for 6 hours. The resulting SiO_2 particles were collected by centrifugation, washed thoroughly with ultrapure water and ethanol, and dried under vacuum.

Fabrication of three-dimensional SiO_2 opal

3D powdered opal was prepared using a self-assembly method based on a sedimentation-assisted centrifugation approach.[2] SiO_2 nanoparticles (1 wt%) were dispersed in ethanol and sonicated for 10 minutes. The particles were sedimented via a centrifugation process at 2000 rpm for 12 minutes. The supernatant was carefully removed, and the sediment was dried under

vacuum. The self-assembled opals were then calcined at 300 ºC for 2 hours to enhance the mechanical stability.

Quantification of methylene blue (MB) in aqueous solution

A standard calibration curve was established to relate the absorbance intensity to the concentration of MB dye for quantitative analysis. MB was initially dissolved in ultrapure water and subsequently diluted to prepare standard solutions with concentrations ranging from 1 to 5 ppm. UV-visible absorption spectra were recorded for each solution, and the absorbance at the characteristic peak wavelength of 667 nm was used to construct the calibration curve.

Quantification of malachite green (MG) in aqueous solution

A standard calibration curve was established to relate the absorbance intensity to the concentration of MG dye for quantitative analysis. MG was initially dissolved in ultrapure water and subsequently diluted to prepare standard solutions with concentrations ranging from 5 to 25 ppm. UV-visible absorption spectra were recorded for each solution, and the absorbance at the characteristic peak wavelength of 620 nm was used to construct the calibration curve.

Quantification of rhodamine 6G (R6G) in aqueous solution

A standard calibration curve was established to relate the absorbance intensity to the concentration of R6G dye for quantitative analysis. R6G was initially dissolved in ultrapure water and subsequently diluted to prepare standard solutions with concentrations ranging from 1 to 6 ppm. UV-visible absorption spectra were recorded for each solution, and the absorbance at the characteristic peak wavelength of 525 nm was used to construct the calibration curve.

Construction of colorimetric calibration curve for MB, MG, and R6G quantification

To quantify the amount of surface-bound dye via image-based analysis, a colorimetric calibration curve was constructed. Aqueous dye solutions with various concentrations were prepared using deionized water. 3mg of SiO_2 inverse opal with void size of 325 nm were immersed in 2.5 mL of each solution and incubated in the dark for 90 minutes to allow equilibrium adsorption. After incubation, the platforms were gently removed, rinsed with deionized water to remove any unbound dye, and air-dried for a few minutes. Optical images of the dye-loaded platforms were captured using a Vivo Y50 smartphone camera under consistent ambient lighting and fixed imaging distance. Image analysis was performed using ImageJ software, with mean pixel intensity values extracted from the red channel (for MB and

MG) and green channel (for R6G) which exhibited the most pronounced contrast in response to dye concentration. The dye intensity was calculated using the normalized red pixel values (for MB and MG) and green pixel values (for R6G) of the platform relative to a white filter paper serving as a consistent background for image comparison. The average red/green intensity was plotted against dye concentration to establish a linear calibration curve. This curve was subsequently used to quantify the concentration of residual dye molecules adsorbed on the platform during photodegradation experiments by correlating the RGB intensity values from time-lapse images with the pre-established linear calibration curve.

Photodegradation of MB, MG, and R6G dyes in the presence of SiO_2 inverse opal platforms

The photocatalytic efficacy of SiO_2 inverse opals with three distinct pore sizes was systematically evaluated via the photodegradation of dye. In each experiment, 5 mg of SiO_2 inverse opal was added to a test tube containing 2.5 mL of dye solution (5 ppm). To establish adsorption-desorption equilibrium, the mixture was stirred at 300 rpm in the dark for 60 min. Subsequently, UV-visible absorption spectroscopy was used to monitor the dye concentration at 15-minute intervals. The adsorption capacity of the MB dye by SiO_2 inverse opal was further evaluated by conducting multiple adsorption cycles with periodic replacement of the dye solution (5ppm) at 30 min intervals until saturation was achieved. After the dark adsorption phase (60 min), the residual dye solution was carefully removed and replaced with 2.5 mL ultrapure water. The samples were then irradiated with a 100 W white LED light source for 2 hours under continuous stirring at 300 rpm to induce photocatalytic degradation. After irradiation, the samples were vacuum-dried, and the resulting color change was analyzed using RGB intensity measurements on their optical images (see next section). To evaluate the recyclability and stability of the SiO_2 inverse opal platforms, the MB adsorption-photodegradation cycle was repeated four times using the same samples. The adsorption and photodegradation efficiencies are calculated as follows:

$$\text{Adsorption efficiency} = \left(\frac{C_0 - C_t}{C_0}\right) \times 100\%$$

$$\text{Adsorption capacity} = \left(\frac{total\ mass_{ads}}{mass_{silica}}\right)$$

$$\text{Photodegradation efficiency} = \left(\frac{C_{ads} - C_{dye}}{C_{ads}}\right) \times 100\%$$

where t is the reaction duration, and C_0 and C_t denote dye concentration at 0 min and t min, respectively. For adsorption capacity, total $mass_{ads}$ denote the total amount of MB adsorbed on the SiO_2 surface till saturation achieved and $mass_{silica}$ is the mass of platform used for adsorption process. C_{ads} represents total concentration of MB molecules pre-adsorbed prior to light irradiation and C_{MB} denote the concentration of MB remaining on the SiO_2 IO platform after 2 h of light irradiation, as determined by RGB intensity analysis.

RGB intensity analysis after MB, MG, and R6G photodegradation

The photodegradation of dye was further monitored through optical imaging. Images of the samples were captured at 60-minute intervals during the photoreaction process. The red/green channel of each image was analyzed using ImageJ software, as it is inversely correlated with dye concentration. For instance, a higher red intensity indicates lower MB and MG concentration and correspondingly denotes a greater extent of photodegradation, whereas lower R6G concentration is reflected by higher green-channel intensity. To quantitatively assess this process, red pixel and green values obtained during the photodegradation experiments were mapped onto the previously established calibration curve, thereby enabling real-time estimation of surface-bound dye concentration. The dye intensity was calculated using the normalized pixel values of the platform relative to a white filter paper serving as a consistent background for image comparison. The calculation was as follows:

$$\text{Dye intensity } (t_n) = \left(\frac{R_{platform}\,(t_n)}{R_{filter}\,(t_n)}\right) - \left(\frac{R_{platform}\,(t_0)}{R_{filter}\,(t_0)}\right)$$

where dye intensity is a proxy for dye concentration, $R_{platform}$ denotes red/green channel pixel intensity of the SiO_2 inverse opal platform, R_{filter} represents red/green channel pixel intensity of the background white filter paper, t_n is the time during the photodegradation experiment, and t_0 is the initial time point before light irradiation. By comparing the normalized intensity to the calibration curve, the amount of degraded dye at each time point was quantified.

Material characterization

Scanning electron microscopy (SEM) characterizations were performed with JEOL-JSM-7600F microscope. UV-visible absorption spectroscopic measurement was conducted with a AvaSpec-ULS2048CL-EVO-UA-50 equipped with a deuterium-halogen light source (AvaLight-DH-S). Diffuse reflectance spectroscopy (DRS) measurement was conducted with AvaSpec-ULS2048CL-EVO-UA-50 and integrating sphere with halogen light source (AvaSphere-50-LS-HAL-12V). Optical images were captured using a Vivo Y50 smartphone

camera. Microscopic images were taken using a Nikkon 406307 upright darkfield microscope imaging system. Angular dependance reflectance measurement was conducted with AvaSpec-ULS4096CL-EVO-UA and zenon light source (Technospex). Attenuated total reflectance-Fourier transform infrared spectroscopy (ATR-FTIR) analysis was conducted using with Perkin-Elmer ATR.

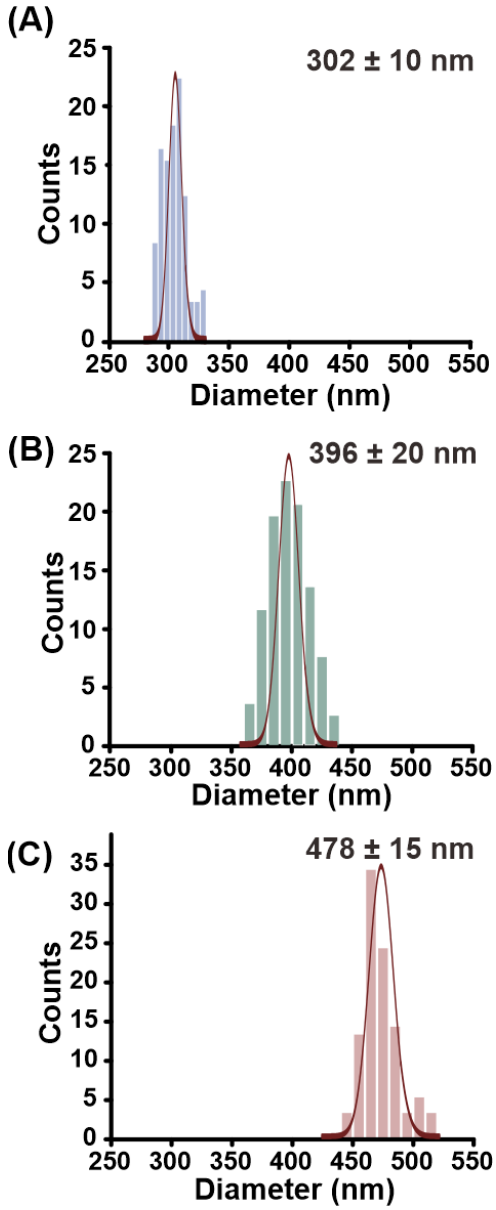

Figure S1. As-synthesized polystyrene (PS) nanoparticles with an average diameter of (A) 302 ± 10 nm, (B) 396 ± 20 nm, and (C) 478 ± 15 nm.

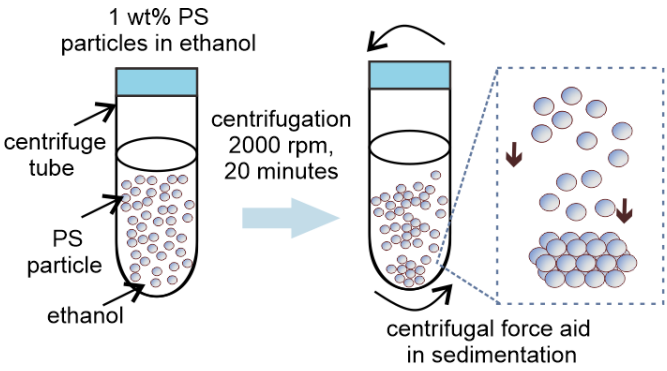

Figure S2. Schematic illustration of the self-assembly process for forming three-dimensional (3D) PS opal powder via a sedimentation-driven approach assisted by centrifugation.

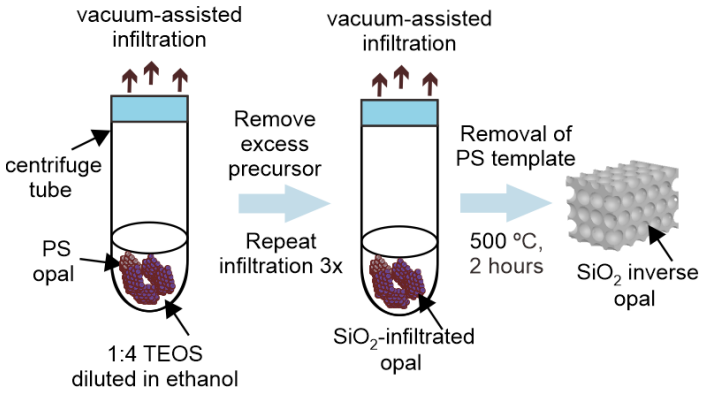

Figure S3. Schematic illustration of the infiltration of SiO_2 precursor into PS opal templates via a vacuum-assisted impregnation method, followed by template removal through thermal calcination to yield SiO_2 inverse opals.

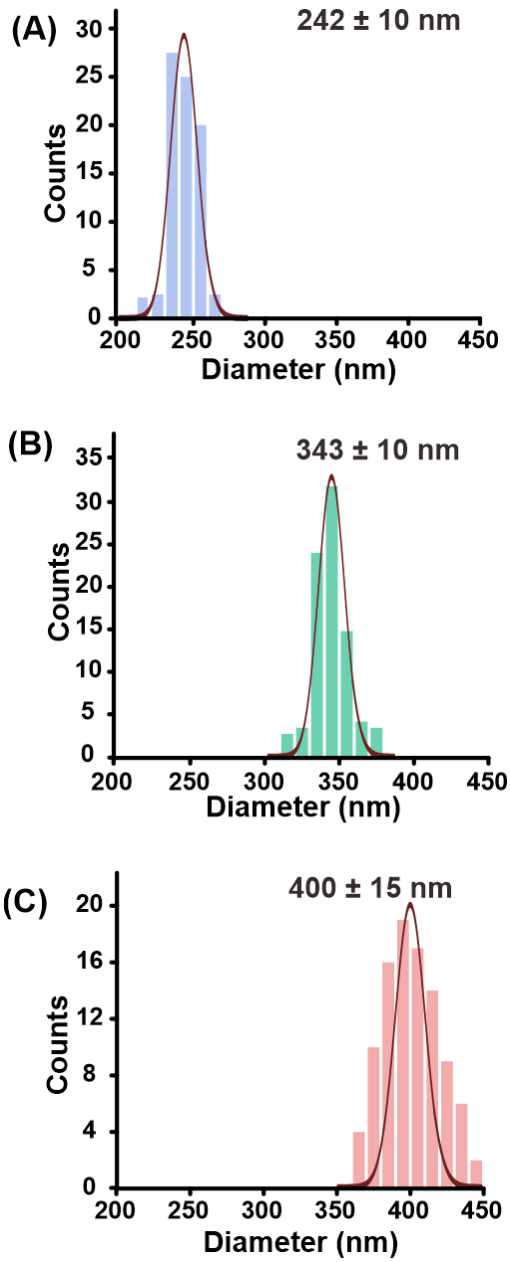

Figure S4. SiO_2 inverse opals with average pore diameters of (A) 242 ± 10 nm, (B) 343 ± 10 nm, and (C) 400 ± 15 nm.

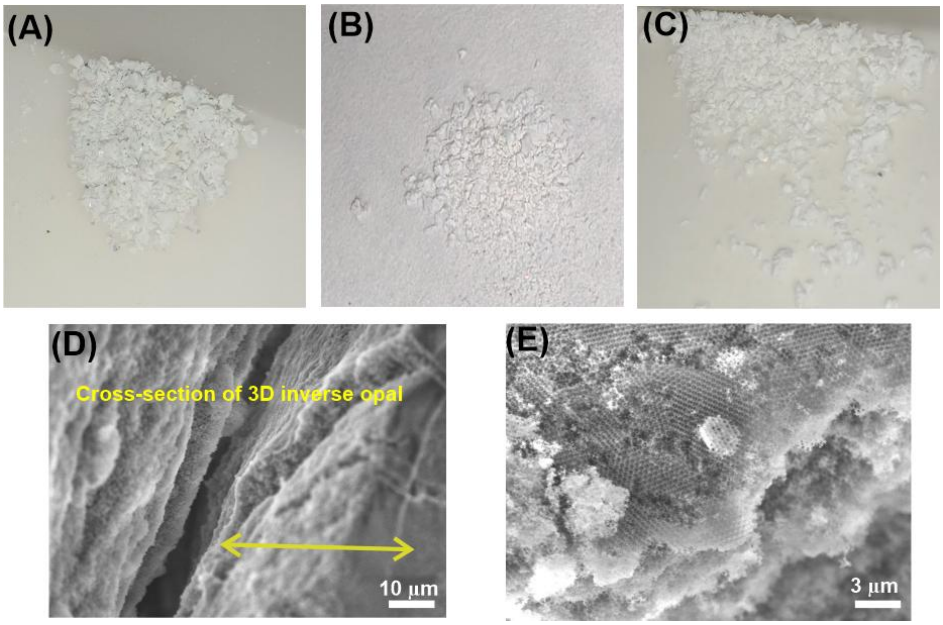

Figure S5. Digital photographs of as-fabricated SiO_2 inverse opals with average pore diameters of (A) 242 ± 10 nm, (B) 343 ± 10 nm, and (C) 400 ± 15 nm. (D) Cross-sectional SEM image of a 3D SiO_2 inverse opal showing a well-ordered multilayer structure extending over more than 100 layers. (E) SEM image showing the periodic arrangement of pores in the inverse opal, indicative of high structural regularity.

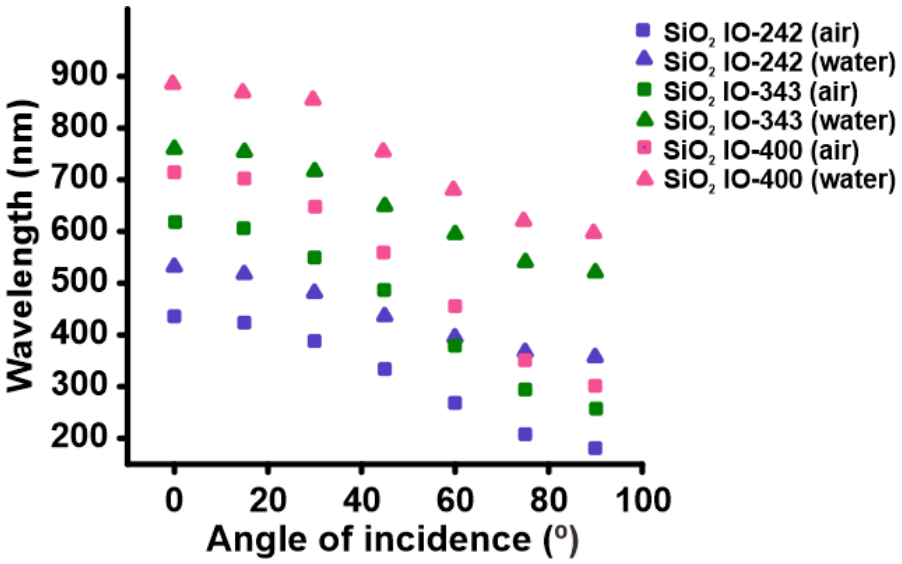

Figure S6. Plot of photonic bandgap (PBG) positions calculated using Bragg's law for SiO_2 IOs in both air and water environments across varying angles of incidence.

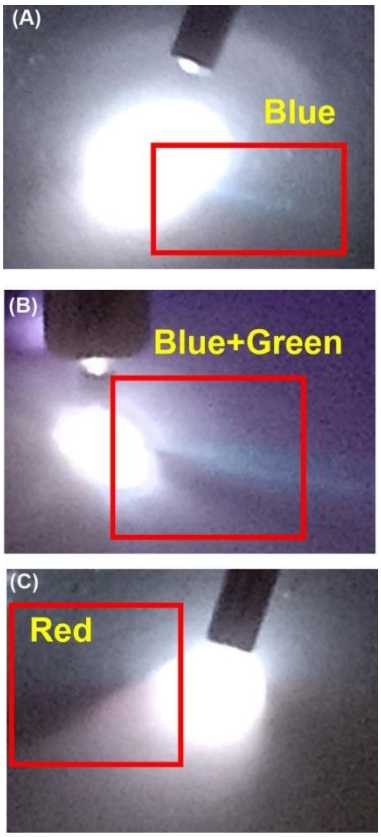

Figure S7. Optical images showing the characteristic stop band reflection of specific light wavelength by various inverse opal photonic crystals upon white light irradiation. (A) SiO_2 IO-242, (B) SiO_2 IO-343, and (C) SiO_2 IO-400.

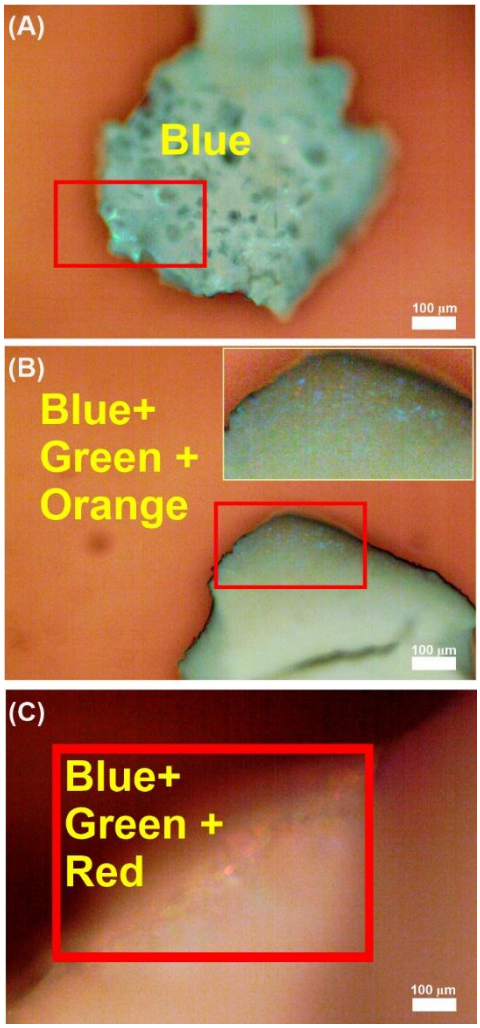

Figure S8. Optical microscopic images illustrating the characteristic stop band reflection exhibited by silica inverse opal photonic crystals under light irradiation. (A) SiO_2 IO-242 and (B) SiO_2 IO-343 are imaged at 50× magnification, while (C) SiO_2 IO-400 is imaged at 100× magnification. The observed structural coloration arises from Bragg diffraction of specific light wavelengths, which is indicative of the photonic bandgap associated with each periodic structure at different angles.

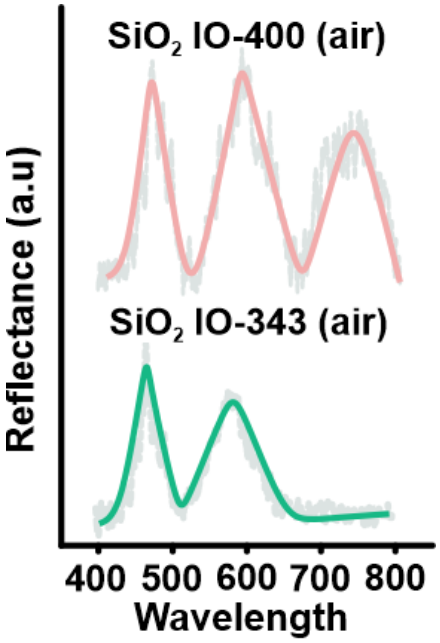

Figure S9. Diffuse reflectance spectra recorded from SiO_2 IO-343 and SiO_2 IO-400 in air medium. Angle-dependent measurements are performed at ~60° relative to the sample surface. The angular dependence of the photonic response in 3D SiO_2 inverse opals contributes to a broadening of light absorption across the visible spectrum with multiple PBG positions due to different exposed angles. Notably, SiO_2 IO-242 was not feasible for measurement because its PBG lies in the range of 180 - 435 nm, which falls outside the detection window of the spectrometer.

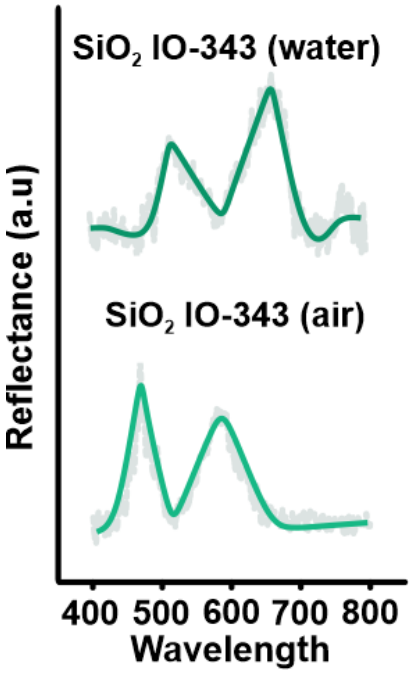

Figure S10. Diffuse reflectance spectra recorded from SiO_2 IO-343 in air and water medium. Angle-dependent measurements are performed at ~60º relative to the sample surface. The angular dependence of the photonic response in SiO_2 IO-343 red-shifted upon measurement in water medium.

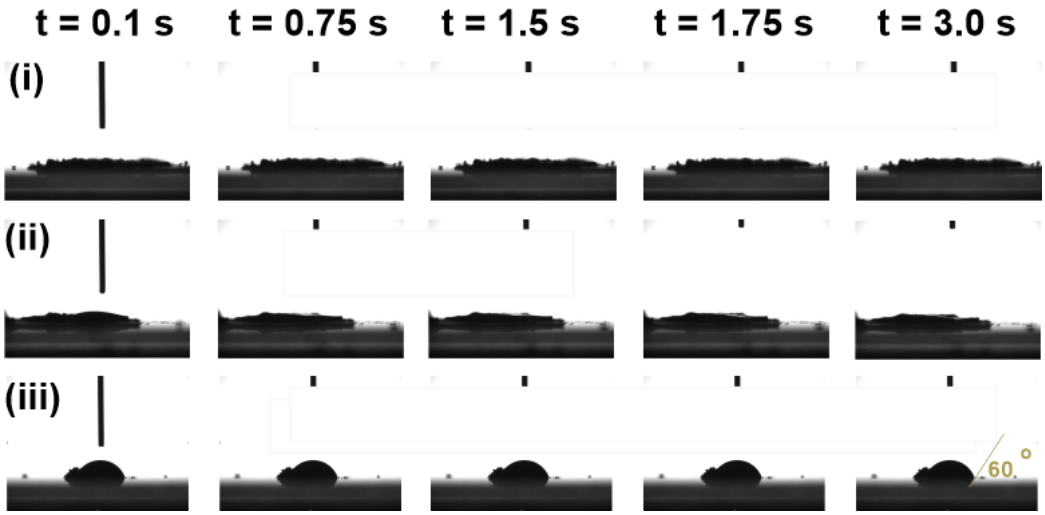

Figure S11. Contact angle measurement of (i) SiO_2 IO-343, (ii) SiO_2 opal-325, and (iii) colloidal SiO_2-325. SiO_2 IO-343 platform exhibits rapid water adsorption, followed by SiO_2 opal-325. Colloidal SiO_2-325 displays the highest contact angle of 60°, indicating the lowest wettability among the three platforms.

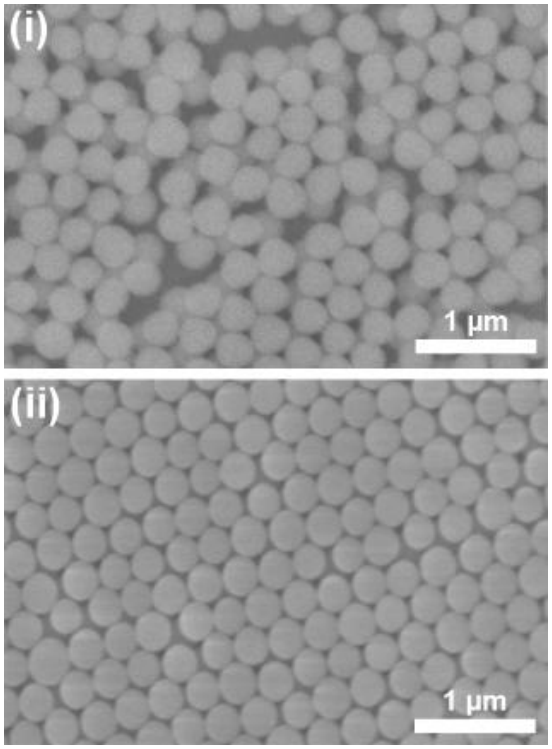

Figure S12. SEM images of (i) colloidal SiO_2 nanoparticles (random arrangement) and (ii) SiO_2 opal with diameter of 345 nm.

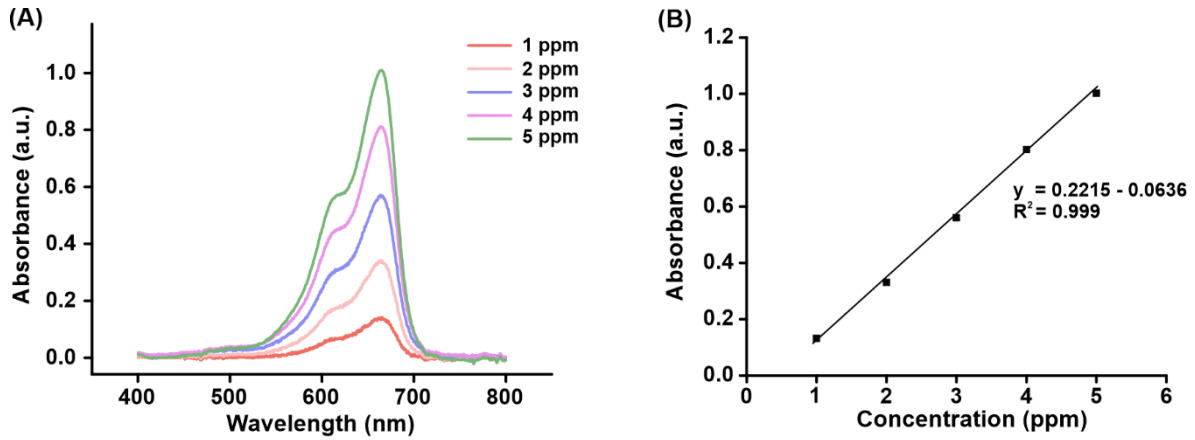

Figure S13. (A) UV-visible absorption spectra and (B) corresponding calibration curve of aqueous MB solution at concentrations ranging from 1 to 5 ppm.

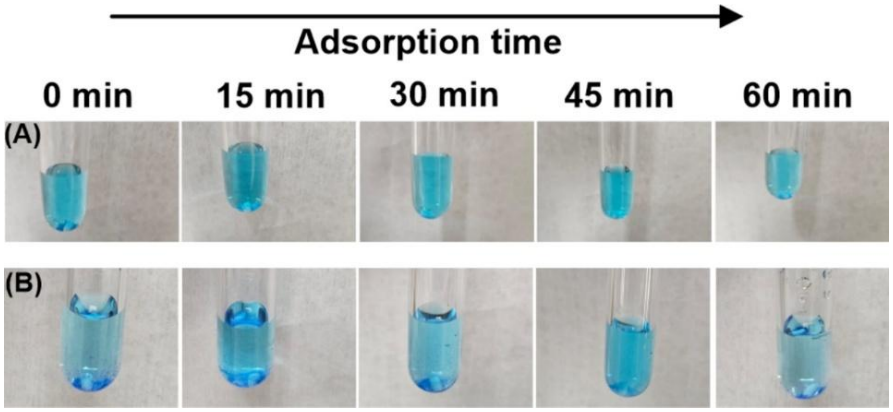

Figure S14. Digital images showing the adsorption process of MB on (A) SiO_2 opal-325 and (B) colloidal SiO_2-325 over 60 min under dark conditions.

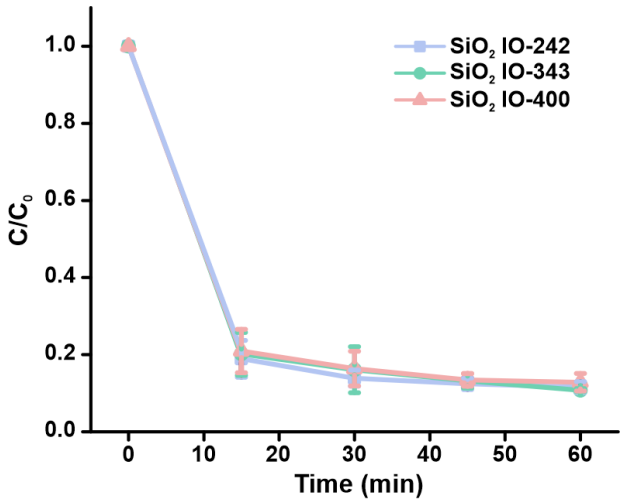

Figure S15. Time-dependent adsorption profiles of MB for SiO_2 inverse opals with pore sizes of 242 nm (SiO_2 IO-242), 343 nm (SiO_2 IO-343), and 400 nm (SiO_2 IO-400) under dark conditions.

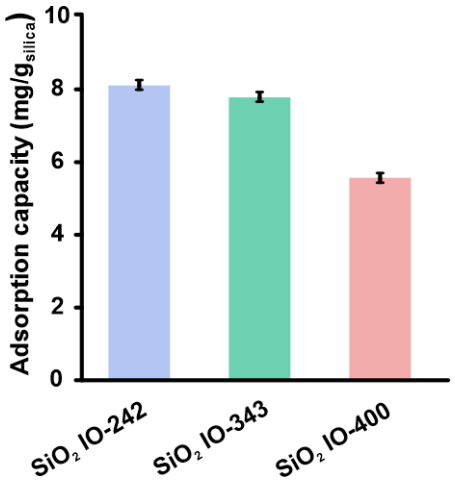

Figure S16. Adsorption capacity of MB on SiO_2 IOs with different periodicities.

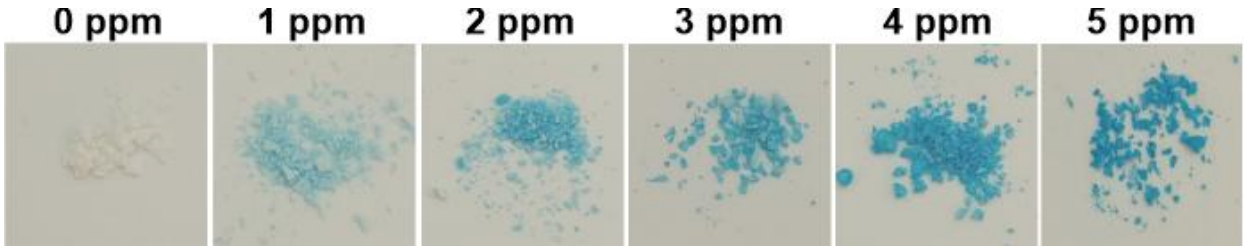

Figure S17. Optical images captured for the calibration of MB absorbance intensity as a function of MB concentration. Calibration curve is generated by plotting red channel intensity (ImageJ) against MB concentration (0 - 5 ppm) adsorbed on the SiO_2 inverse opal platform. The linear correlation serves as a reference for quantifying MB removal during photodegradation experiments.

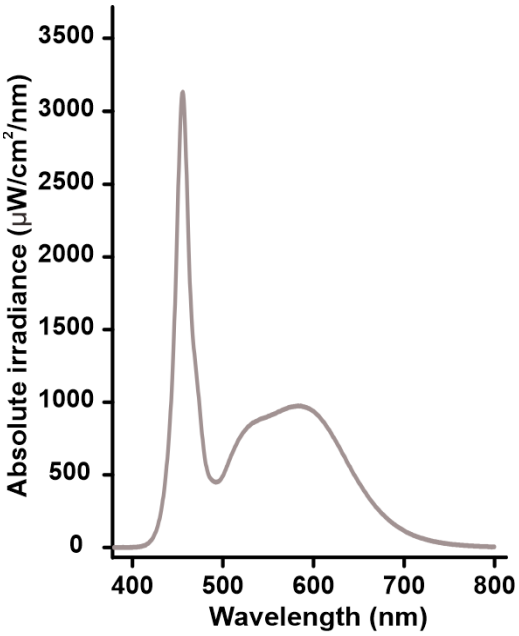

Figure S18. Irradiance spectra of the white LED lamp (100W).

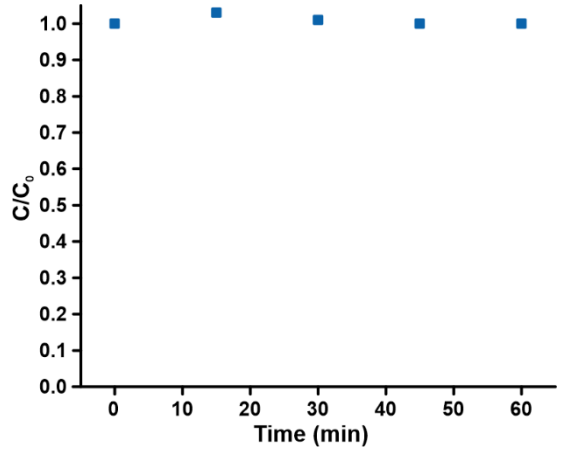

Figure S19. Time-dependent concentration profile of MB under dark conditions in the absence of any particle platforms, showing intrinsic molecule stability and minimal degradation over time.

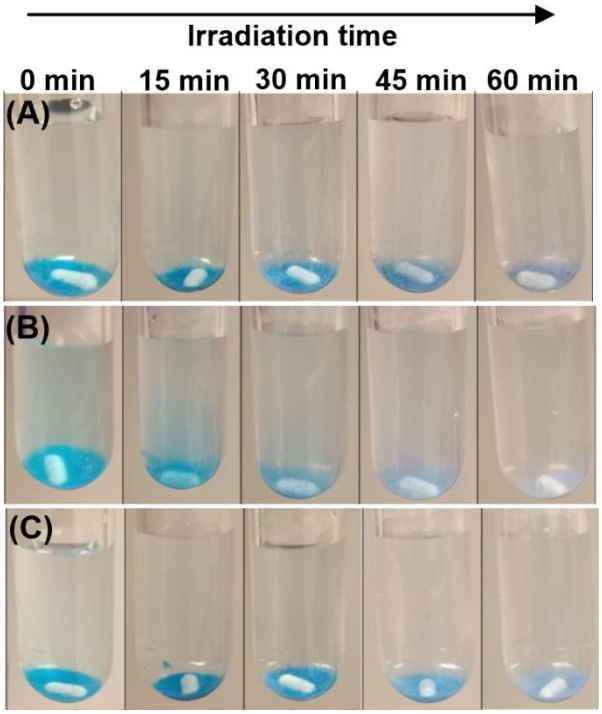

Figure S20. Digital images illustrating the photodegradation of pre-adsorbed MB on (A) SiO_2 IO-242, (B) SiO_2 IO-343, and (C) SiO_2 IO-400 after 60 min of light irradiation.

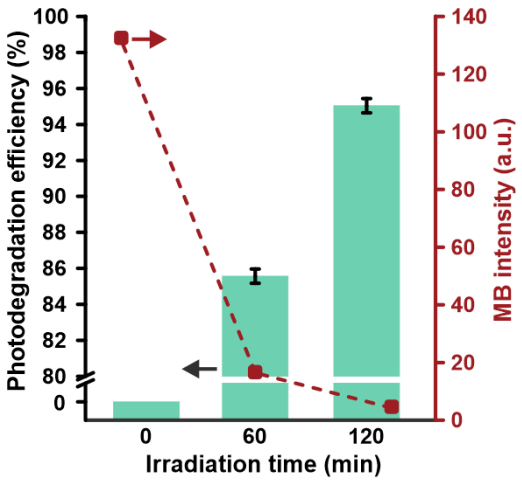

Figure S21. Plot depicting the relationship between photodegradation efficiency and MB intensity values for SiO_2 IO-343 at 60-minute and 120-minute intervals under white light irradiation.

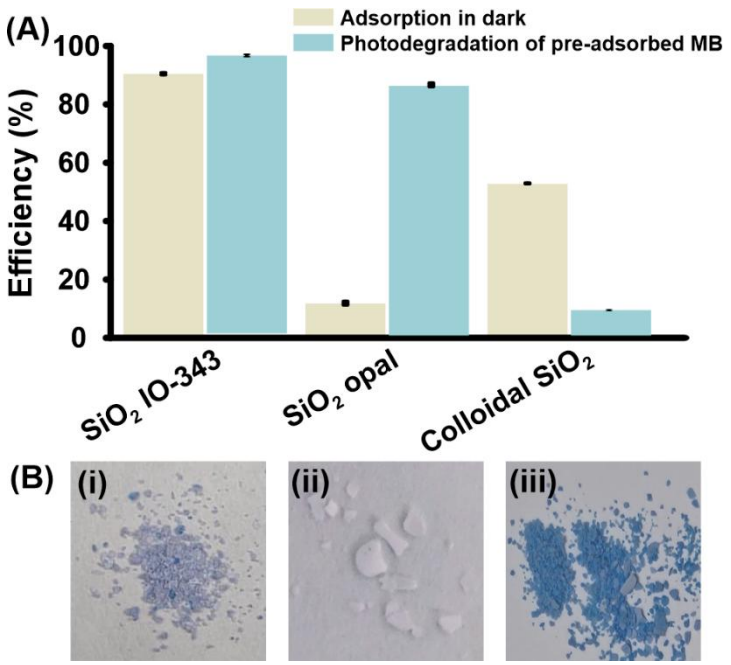

Figure S22. (A) Plot showing the relationship between adsorption and photodegradation efficiencies for various platforms under 1 h of dark conditions and light irradiation, respectively. Photodegradation efficiency is calculated based on the fraction of pre-adsorbed MB molecules degraded under light exposure. (B) Digital images of (i) SiO_2 IO-343, (ii) SiO_2 opal, and (iii) colloidal SiO_2 after 1 h of photoreaction using white light irradiation.

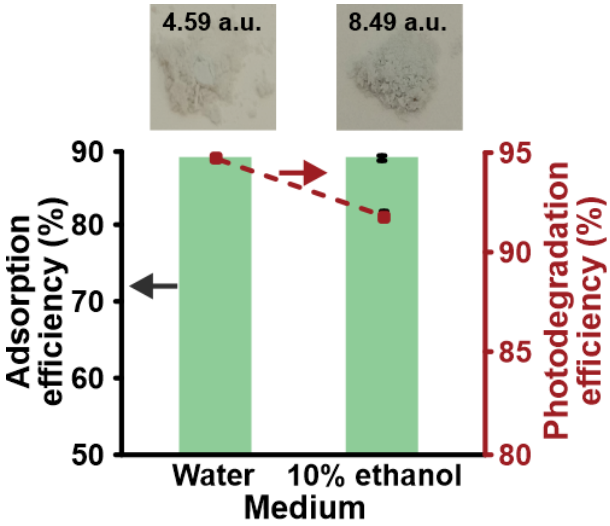

Figure S23. Adsorption and photodegradation efficiency of SiO_2 IO-343 after 120 min of light irradiation in water and 10% ethanol media. Insets, corresponding images of photobleached samples.

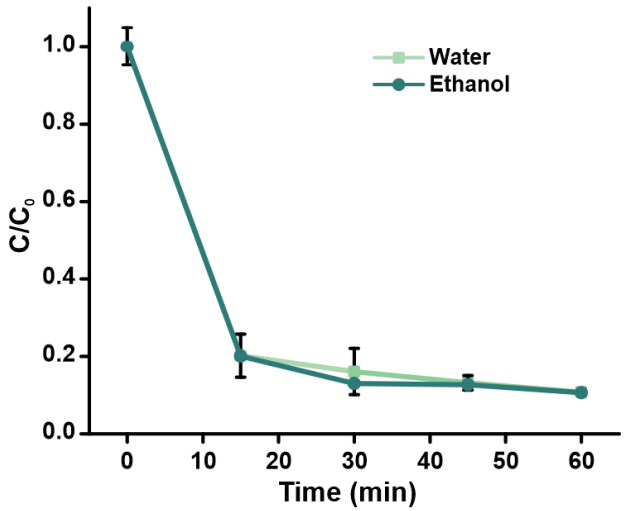

Figure S24. Time-dependent adsorption profiles of MB for SiO_2 IO-242, SiO_2 IO-343, and SiO_2 IO-400 in water and ethanol media.

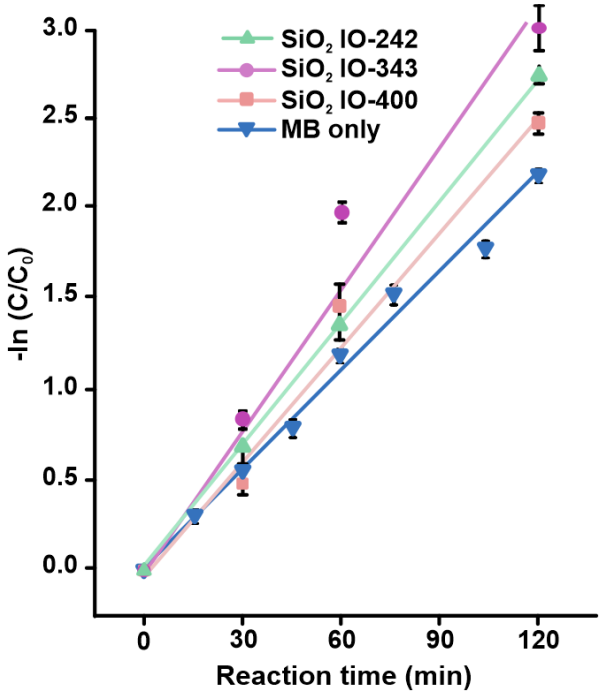

Figure S25. Time-dependent plots of $-\ln(C/C_0)$ for MB photodegradation using SiO_2 inverse opals with different periodicities. MB only denotes intrinsic molecular photobleaching in the absence of any particle platforms.

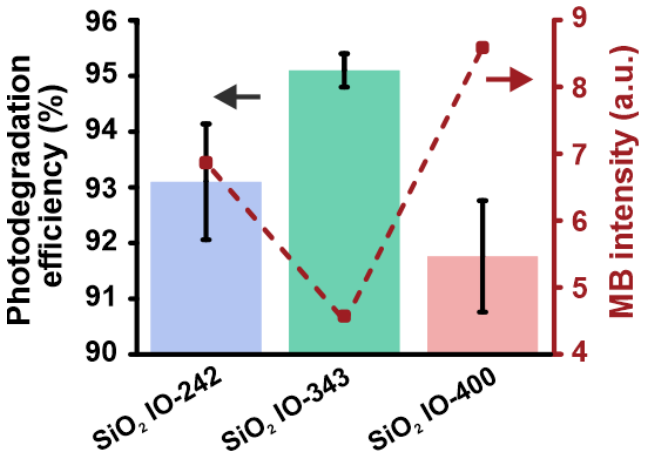

Figure S26. Plot showing the relationship between MB photodegradation efficiency and MB intensity values for SiO_2 IO-242, SiO_2 IO-343, and SiO_2 IO-400 after 2 h of light irradiation (1 cycle).

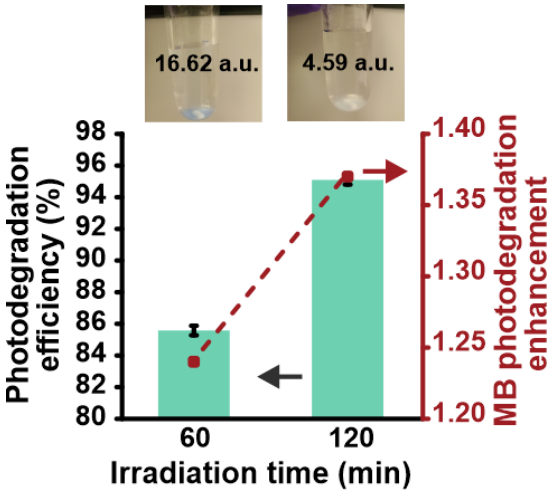

Figure S27. Photodegradation efficiency for SiO_2 IO-343 after 60 min and 120 min of light irradiation. Insets, optical images showing the visual changes in sample color.

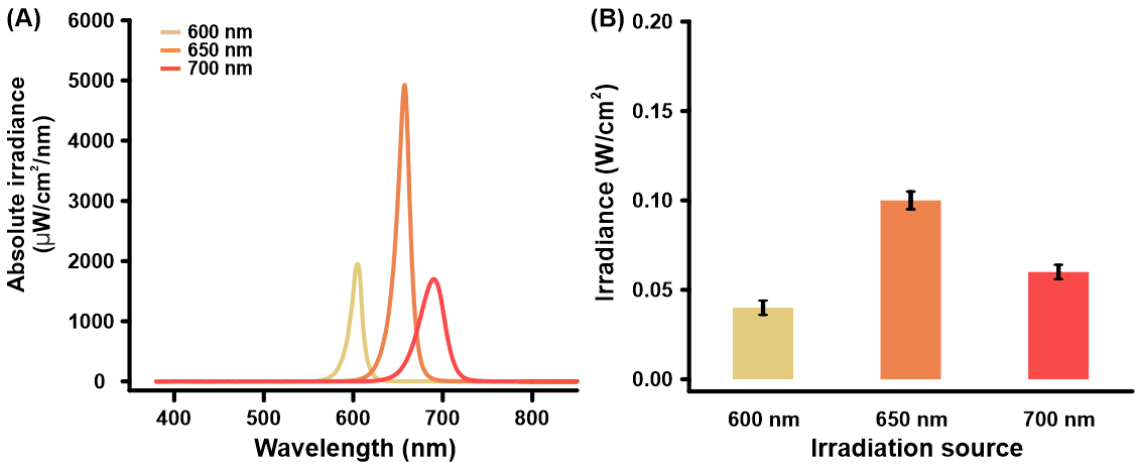

Figure S28. (A) Irradiance spectra of various monochromatic light and (B) the corresponding irradiance.

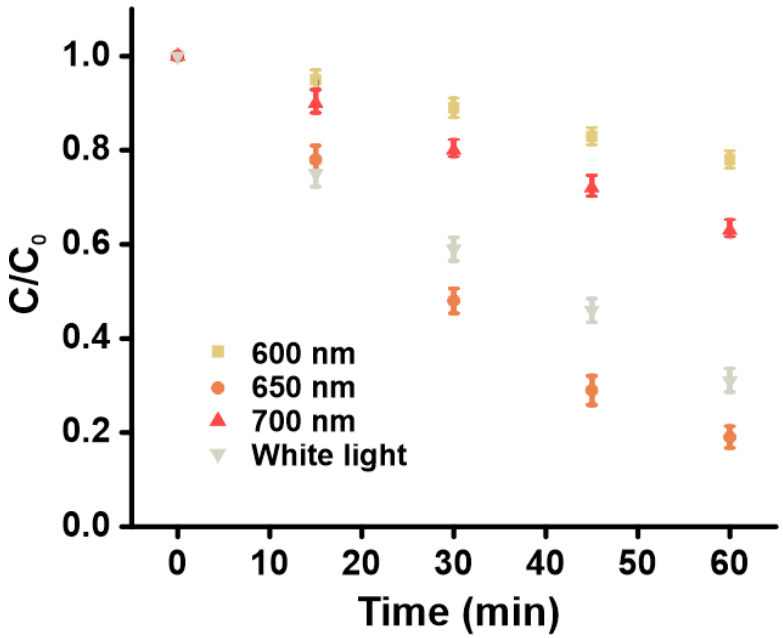

Figure S29. Intrinsic MB photobleaching under monochromatic light irradiation at 600 nm, 650 nm, 700 nm, and white light.

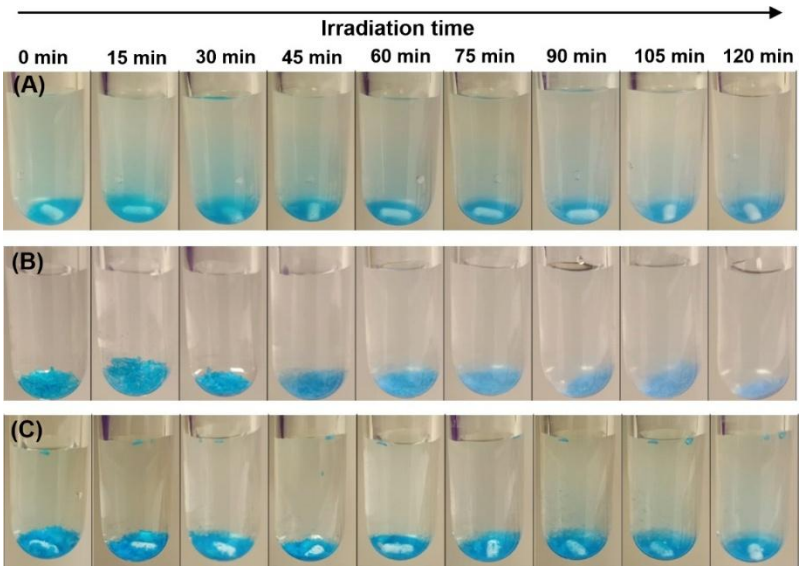

Figure S30. Digital images showing the photodegradation of pre-adsorbed MB on SiO_2 IO-343 over 2 h irradiation (1 cycle) under monochromatic light sources of (A) 600 nm, (B) 650 nm, and (C) 700 nm.

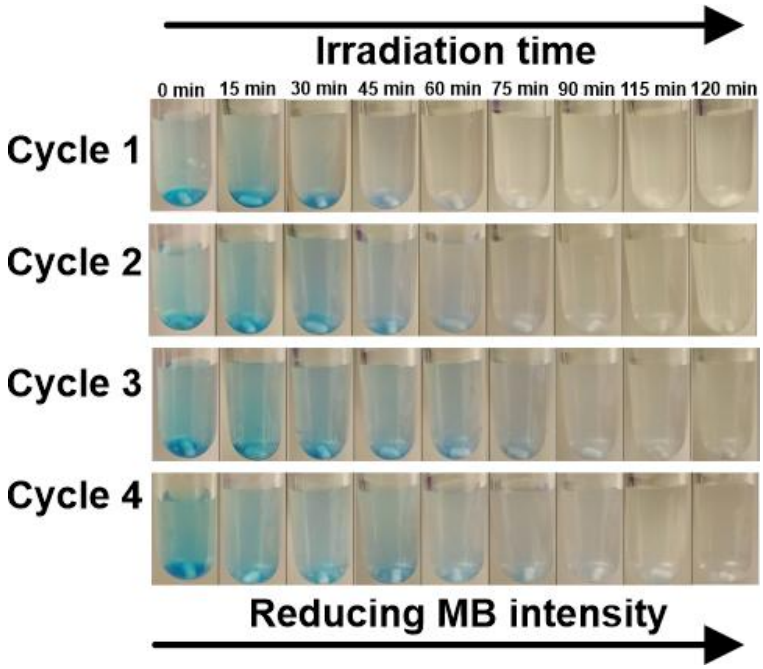

Figure S31. Time-resolved digital images showing the progressive photodegradation of pre-adsorbed MB on SiO_2 IO-343 across four reaction cycles.

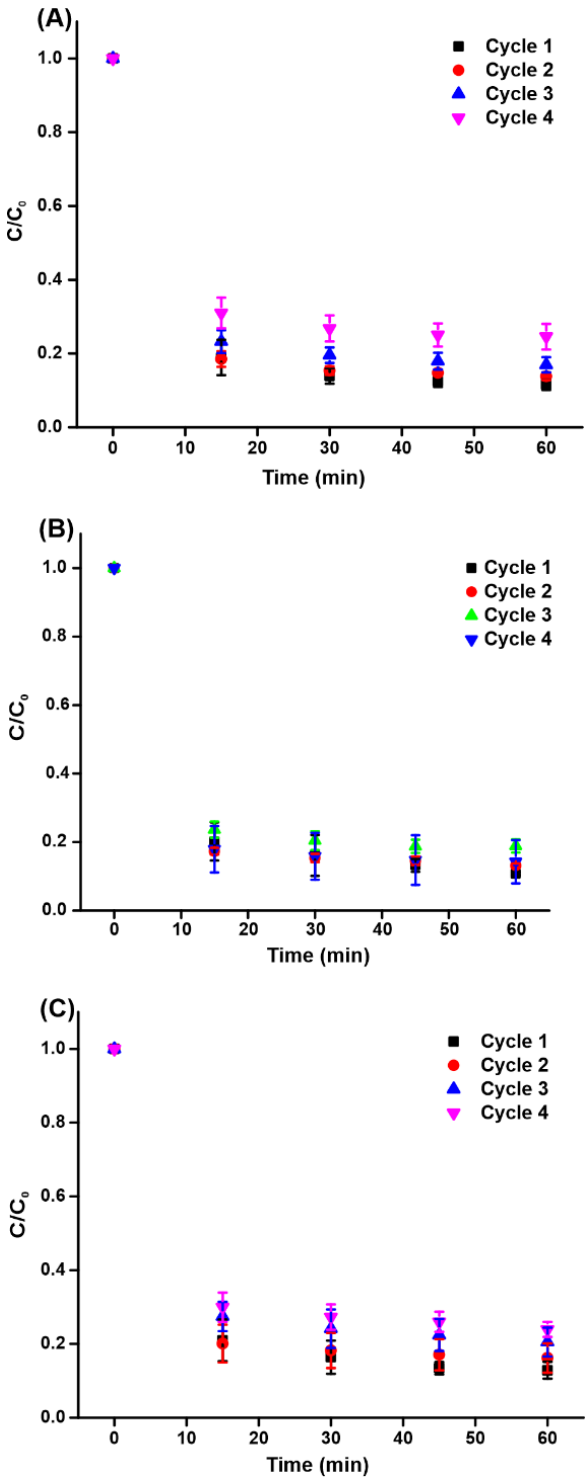

Figure S32. Time-dependent adsorption profiles of MB on SiO_2 IO-242, SiO_2 IO-343, and SiO_2 IO-400 over four consecutive reaction cycles.

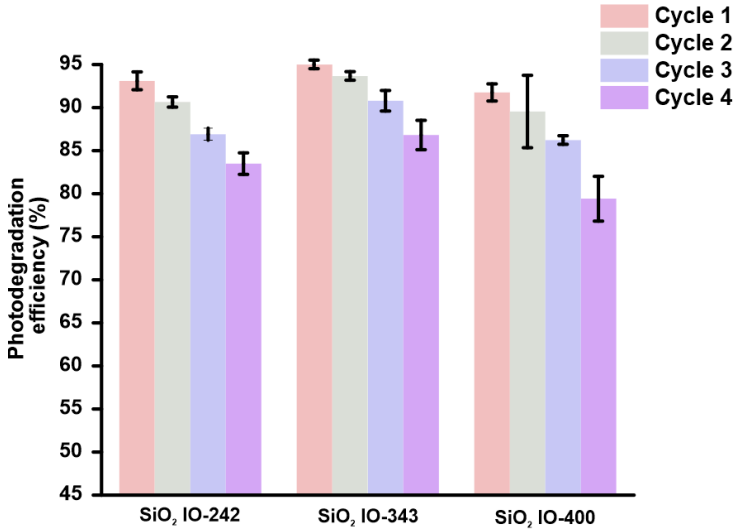

Figure S33. Recyclability performance of all platforms over four consecutive reaction cycles. Each cycle consists of 1 h of MB adsorption under dark conditions, followed by 2 h of light irradiation for photodegradation.

Supporting text 1

To evaluate the generality of the SiO_2 IO toward other organic dyes beyond MB, we selected malachite green (MG) and rhodamine 6G (R6G) as representative commercial dyes and employed SiO_2 IO-343 as the model platform. These dyes were chosen due to their widespread use, distinct molecular sizes, and different adsorption behaviours on silica surfaces. SiO_2 IO-343 was immersed in a 5 ppm of respective dye solution in the dark for 60 min to isolate the adsorption process and exclude any contributions from light-induced degradation. We extract aliquots of the sample solution at pre-defined time intervals over a 15-min period to quantify the remaining pollutant using MG and R6G absorption peak at 620 nm and 535 nm, respectively, and a standard calibration curve via UV-visible absorption spectroscopy (Figure S34, S35). Quantitative UV-visible absorption analysis further confirms that SiO_2 IO-343 adsorbs 90% of MB, 87% of MG, and 79.7% of R6G within 60 min, indicating stronger adsorption toward MB and MG compared to the R6G molecules (Figure S36, S37). The slightly reduced adsorption of R6G can be attributed to its bulkier molecular structure, which features a larger xanthene framework and steric hindrance from ethyl substituents, limiting its accessibility to surface silanol sites and internal pore walls. In contrast, MB and MG possess comparatively smaller and more planar structures, allowing more effective electrostatic interaction and surface contact with the negatively charged silica framework.

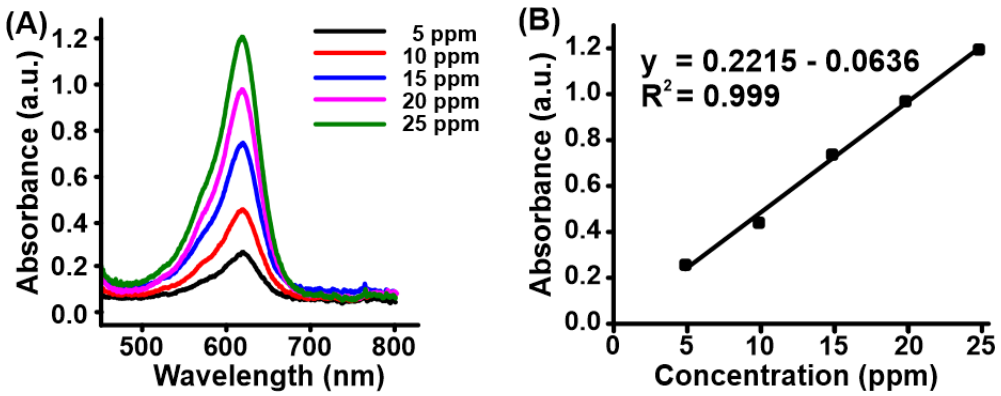

Figure S34. (A) UV-visible absorption spectra and (B) corresponding calibration curve of aqueous MG solution at concentrations ranging from 5 to 25 ppm.

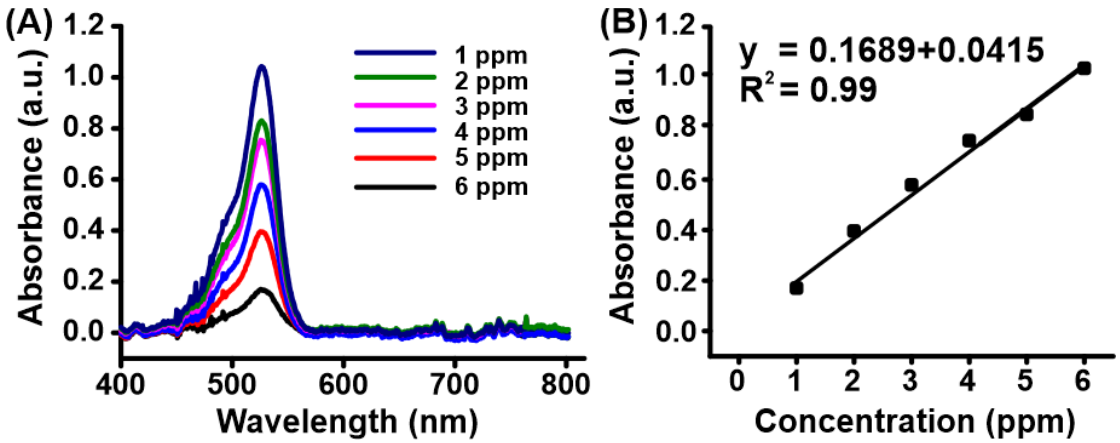

Figure S35. (A) UV-visible absorption spectra and (B) corresponding calibration curve of aqueous R6G solution at concentrations ranging from 1 to 6 ppm.

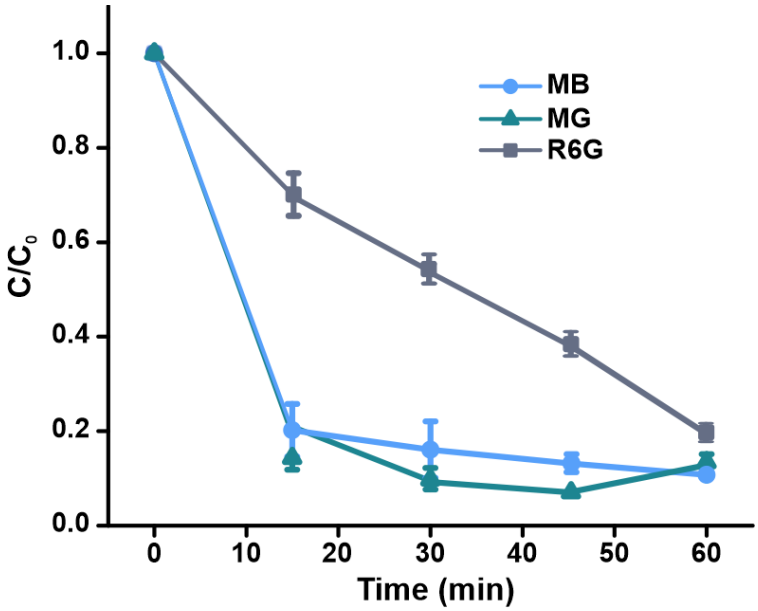

Figure S36. Time-dependent adsorption profiles of MB, MG, and R6G on SiO_2 inverse opals with pore sizes of 343 nm (SiO_2 IO-343) under 60 min of dark conditions.

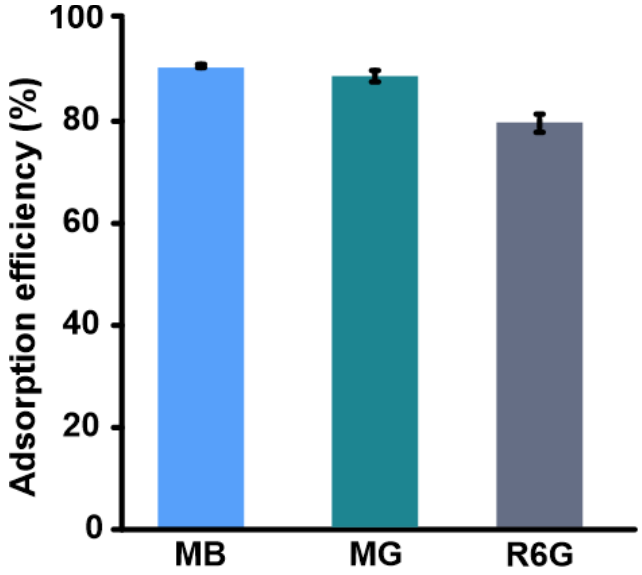

Figure S37. Comparison of adsorption efficiency of MB, MG, and R6G pollutants on SiO_2 inverse opals with pore sizes of 343 nm (SiO_2 IO-343) under 60 min dark conditions.

Supporting text 2

We next assess their ability to mediate light-induced pollutant degradation. To enable quantitative evaluation of pollutant removal, a colorimetric calibration curve is established by allowing the SiO_2 inverse opal to adsorb MG and R6G from aqueous solutions with different concentrations (Figure S38, S39). Optical images of the platform are captured after equilibration at each concentration and RGB intensity values are extracted to generate the calibration curve of MG and R6G intensity index (Figure S40, S41). This process enables subsequent image-based quantification of pollutant concentration during visible light irradiation. Among the tested organic pollutants, SiO_2 IO-343 exhibits the most pronounced decolorization of the pre-adsorbed MG upon light irradiation. Its initially intense appearance (MG intensity ~98 a.u.) fades markedly under light exposure, reaching 34.56 a.u. after 120 minutes which corresponds to a photodegradation efficiency of 68% (Figure S42). Interestingly, kinetic analysis using the integrated first-order rate law, $-\ln(C/C_0) = k_{app} \cdot t$, reveals that SiO_2 IO-343 exceeds the intrinsic MG photobleaching by 10-fold (Figure S43, S44). In the case of R6G pollutant, SiO_2 IO-343 achieves a photodegradation efficiency of 46% (R6G intensity from ~40 a.u. to ~21 a.u.) and demonstrates improvement in photodegradation kinetics of ~1.7-fold compared to R6G intrinsic photobleaching (Figure S45-47).Systematic comparisons of the optical profiles of the photonic crystals and MG's absorption spectrum attribute SiO_2 IO-343's enhanced photodegradation capability to the strongest spectral overlap between its PBG slow photons and MG's absorption band at 620 nm (Figure S48). In contrast, SiO_2 IO-343 possess PBGs (Table S3) that are partially aligned with absorption region of R6G at 535 nm, thereby demonstrating relatively weaker improvements in photodegradation kinetics. Overall, these results demonstrate that the SiO_2 inverse opal platform can effectively photodegrade organic pollutants beyond MB by leveraging wavelength selective slow photon enhancement, highlighting its versatility and tunability for broader photocatalytic applications.

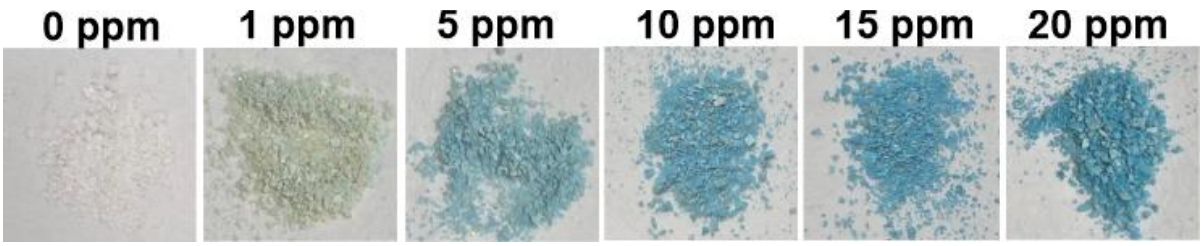

Figure S38. Optical images captured for the calibration of MG absorbance intensity as a function of MG concentration. Calibration curve is generated by plotting red channel intensity (ImageJ) against MG concentration (0 - 20 ppm) adsorbed on the SiO_2 inverse opal platform. The linear correlation serves as a reference for quantifying MG removal during photodegradation experiments

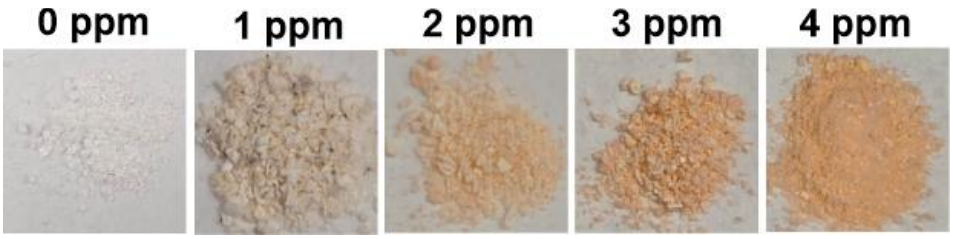

Figure S39. Optical images captured for the calibration of R6G absorbance intensity as a function of R6G concentration. Calibration curve is generated by plotting green channel intensity (ImageJ) against MG concentration (0 - 4 ppm) adsorbed on the SiO_2 inverse opal platform. The linear correlation serves as a reference for quantifying R6G removal during photodegradation experiments.

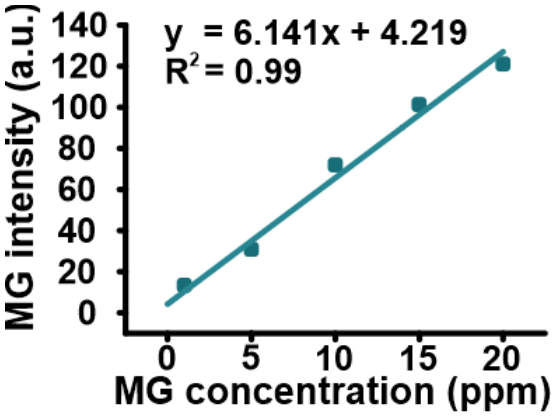

Figure S40. Calibration curve of MG absorbance intensity as a function of MG concentration.

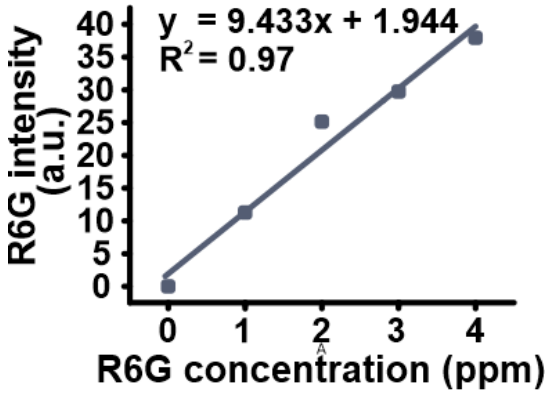

Figure S41. Calibration curve of R6G absorbance intensity as a function of R6G concentration.

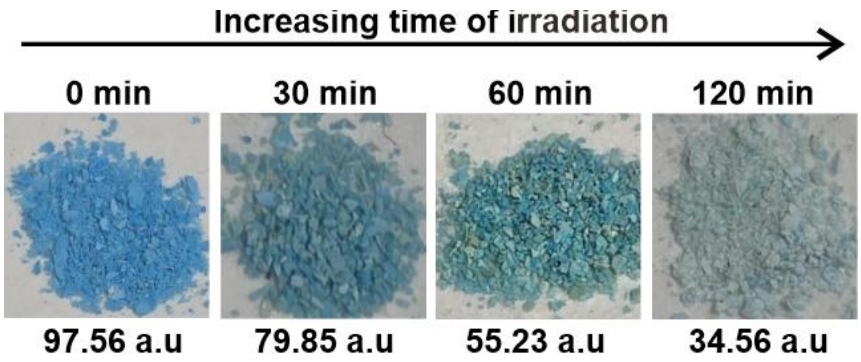

Figure S42. Digital images showing the progressive photodegradation of pre-adsorbed MG on SiO_2 IO-343 across 2 h of light irradiation.

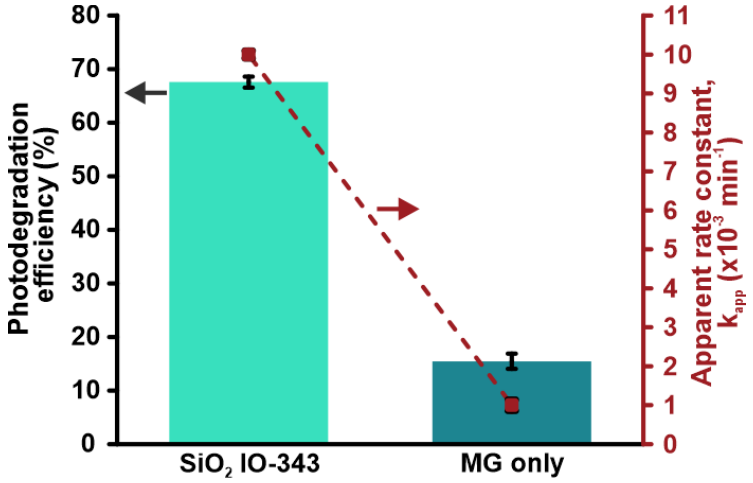

Figure S43. Comparison of photodegradation efficiency and apparent rate constants (k_{app}) representing the MG's photobleaching kinetics across SiO_2 IO-343 and MG-only control after 2 h of light irradiation.

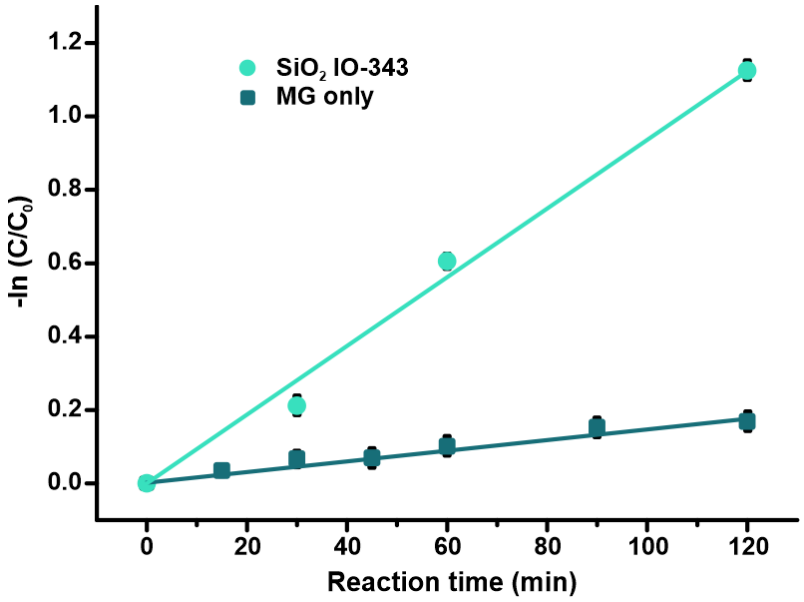

Figure S44. Time-dependent plots of -ln(C/C0) for MG photodegradation using SiO_2 inverse opals with different periodicities. MG only denotes intrinsic molecular photobleaching in the absence of any particle platforms.

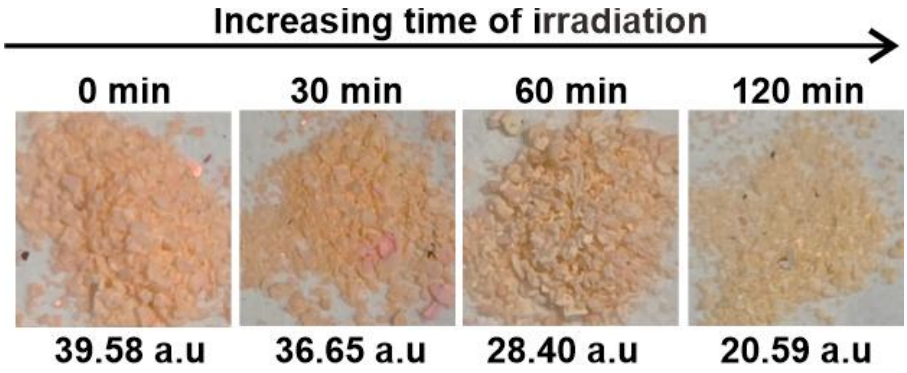

Figure S45. Digital images showing the progressive photodegradation of pre-adsorbed R6G on SiO_2 IO-343 across 2 h of light irradiation.

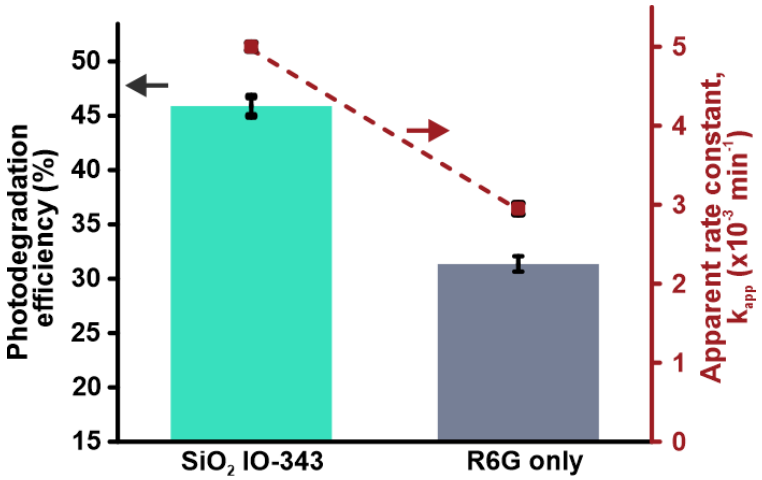

Figure S46. Comparison of photodegradation efficiency and apparent rate constants (k_{app}) representing the R6G's photobleaching kinetics between SiO_2 IO-343 and R6G-only control after 2 h of light irradiation.

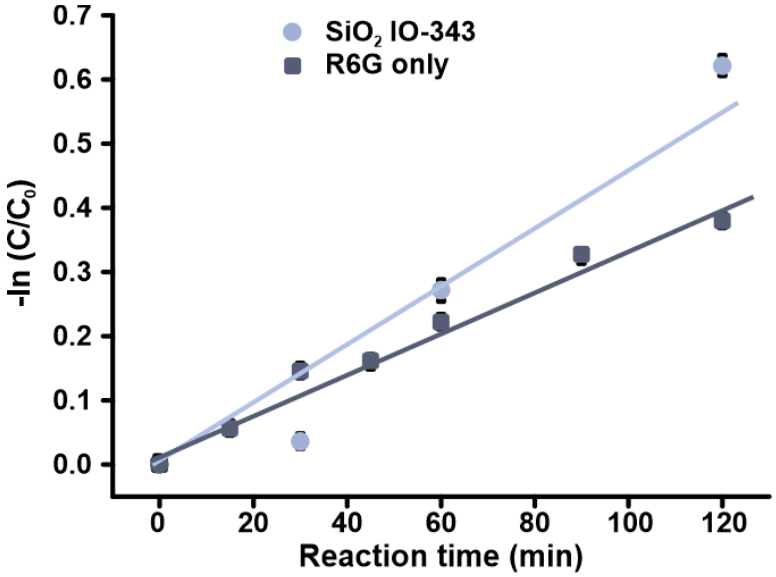

Figure S47. Time-dependent plots of $-\ln(C/C_0)$ for R6G photodegradation using SiO_2 inverse opals with different periodicities. R6G only denotes intrinsic molecular photobleaching in the absence of any particle platforms.

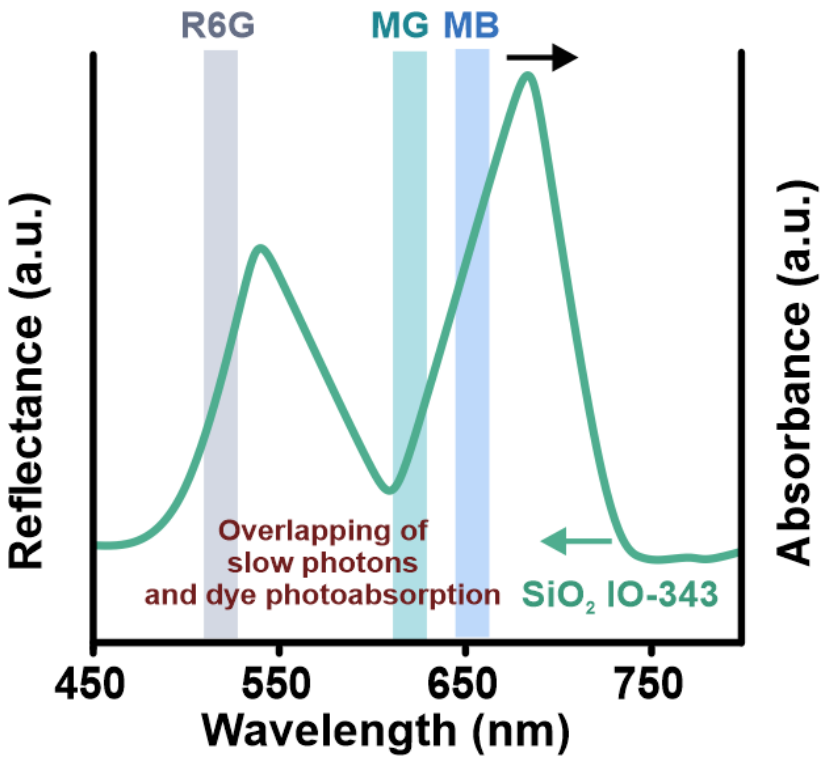

Figure S48. Reflectance spectrum of SiO_2 IO-343 and absorption regions of MB, MG, and R6G**.**

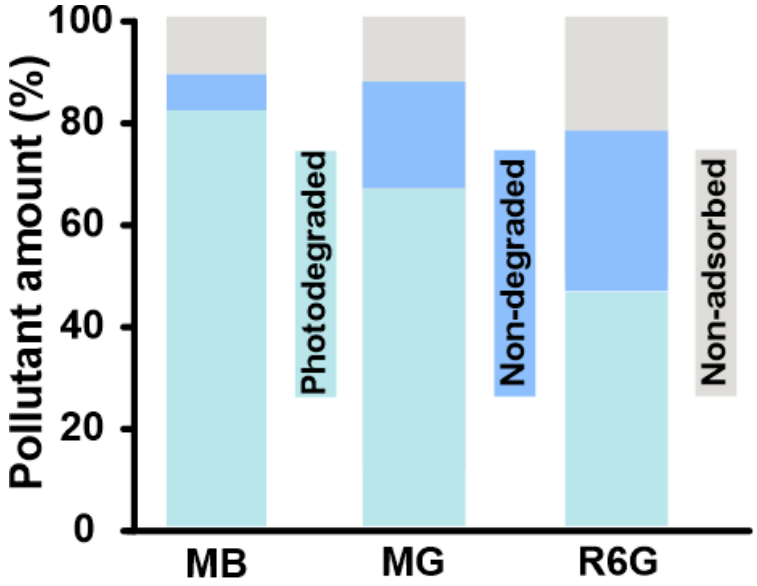

Figure S49. Percentage of different pollutant removal, accounting for adsorption, photodegradation, and residual (non-degraded) content by using SiO_2 IO-343. A typical experiment involves 1h of pollutant adsorption under dark conditions followed by 2 h of visible light irradiation.

Table S1. Percentage of shrinkage in SiO_2 IOs relative to their corresponding PS opal templates.

	SiO_2 IO-242		**SiO_2 IO-343**		**SiO_2 IO-400**	
	PS opal	**SiO_2 IO**	**PS opal**	**SiO_2 IO**	**PS opal**	**SiO_2 IO**
Diameter (nm)	302	242	396	343	478	400
% of shrinkage	19.8		13.4		16.3	

Table S2. Calculated PBG values for each SiO_2 inverse opal-based photonic crystals in air medium.

Angle (º) / Diameter (nm)	242	343	400
0	435.93	617.09	719.41
15	423.67	599.73	699.173
30	388.20	549.53	640.64
45	333.71	472.40	550.72
60	268.38	379.92	442.91
75	207.93	294.34	343.14
90	180.82	255.96	298.40

Calculation of PBG position based on Bragg's law.

$$\lambda_{max} = (8/3)^{1/2} D (n^2_{eff} - \sin^2 \theta)^{1/2}$$

where λ_{max} is the wavelength of stop band maximum, D is the diameter of the spheres, n_{eff} is the effective refractive index, and θ is the angle between the incident and the reflective surface.

Since the photonic crystal adopts a FCC crystal structure, SiO_2 and air medium occupy 22% and 78% of the total space, respectively.

The refractive indices of SiO_2 and air are: n of SiO_2 = 1.45 and air = 1.00

$n^2_{eff} = [(0.78 \times 1.00) + (0.22 \times 1.45)]^2 = 1.21$

At $\theta = 90^o$, $\sin^2 90^o = 1$

For SiO_2 inverse opal with diameter of 242 nm at light irradiation angle of 90º in air medium,

$\lambda_{max} = (8/3)^{1/2}\ 242\ (1.21\text{-}1)^{1/2}$

$\lambda_{max} = 180.82$ nm

Table S3. Calculated PBG values for each SiO_2 inverse opal-based photonic crystals in water medium.

Angle (º) / diameter (nm)	242	343	400
0	538.03	761.62	887.90
15	528.14	747.63	871.89
30	500.14	707.99	825.38
45	459.14	649.94	757.71
60	414.09	586.18	683.37
75	377.73	534.70	623.35
90	363.51	514.57	599.89

Calculation of PBG position based on Bragg's law.

$$\lambda_{max} = (8/3)^{1/2} D (n^2_{eff} - \sin^2 \theta)^{1/2}$$

where λ_{max} is the wavelength of stop band maximum, D is the diameter of the spheres, n_{eff} is the effective refractive index, and θ is the angle between the incident and the reflective surface.

Since the photonic crystal adopts a FCC crystal structure, SiO_2 and air medium occupy 22% and 78% of the total space, respectively.

The refractive indices of SiO_2 and water are: n of SiO_2 = 1.45 and water = 1.33

$n^2_{eff} = [(0.78 \times 1.33) + (0.22 \times 1.45)]^2 = 1.84$

At $\theta = 90^o$, $\sin^2 90^o = 1$

For SiO_2 inverse opal with diameter of 242 nm at light irradiation angle of 90º in air medium,

$\lambda_{max} = (8/3)^{1/2}\ 242\ (1.84\text{-}1)^{1/2}$

$\lambda_{max} = 363.51$ nm

Table S4. Calculated PBG values for each SiO_2 opal-based photonic crystals in water medium.

Angle (º) / diameter (nm)	325
0	753.6
15	741.0
30	705.4
45	653.5
60	597.2
75	552.4
90	535.1

Calculation of PBG position based on Bragg's law.

$$\lambda_{max} = (8/3)^{1/2} D (n^2_{eff} - \sin^2 \theta)^{1/2}$$

where λ_{max} is the wavelength of stop band maximum, D is the diameter of the spheres, n_{eff} is the effective refractive index, and θ is the angle between the incident and the reflective surface.

Since the photonic crystal adopts a FCC crystal structure, SiO_2 spheres and air medium occupy 75% and 25% of the total space, respectively.

The refractive indices of SiO_2 and water are: n of SiO_2 = 1.45 and water = 1.00

$n^2_{eff} = [(0.75 \times 1.45) + (0.25 \times 1.33)]^2 = 2.01$

At $\theta = 90^o$, $\sin^2 90^o = 1$

For SiO_2 opal with diameter of 325 nm at light irradiation angle of 90º in water medium,

$\lambda_{max} = (8/3)^{1/2} 325 (2.01\text{-}1)^{1/2}$

$\lambda_{max} = 535.1$ nm

Table S5. Comparison of the photodegradation performance of the SiO_2 inverse opal (IO)-based platform developed in this work with other reported photocatalytic systems.

Photonic Crystals	Catalyst dosage (g)	Light source	k_{app} (min^{-1})	Photodegradation efficiency	References
Cd-MOF/CdS	10mg	simulated sunlight	0.023	91.9% (100 min)	4
Au-TiO_2-NAA-DBRs	$1cm^2$	simulated solar light	0.024	-	5
10 wt% WO_3/TiO_2	30mg	Halogen lamp (400 W)	0.017	98.92% (180 min)	6
TiO_2 IOPM	film	simulated sunlight--Xenon lamp (500 W)	-	60% (90 min)	7
IO–TiO_2	$1cm^2$ film	visible light	0.002	85% (14h)	8
IO–TiO_2–Au	$1cm^2$ film	visible light	0.005	95% (7h)	8
TiO_2 IO films	$1cm^2$ film	UV lamp at 365 nm	0.004	42% (2h) 90% (10h)	9
Co-TiO_2 IO PC	10 mg	simulated sunlight--Xenon lamp (500 W)	0.021	75% (60 min)	10
TiO_2 IO PC	10 mg	simulated sunlight--Xenon lamp (500 W)	0.014	60% (60 min)	10
SiO_2 IO-343	**5mg**	**white light (100 W)**	**0.027**	**95.10% (120 min)**	**Our study**
SiO_2 IO-343	**5mg**	**white light (100 W)**	**0.033**	**85.9% (60 min)**	**Our study**

References

1. J.-F. Fang, Y.-M. Xuan, Q. Li, *Sci. China Technol. Sci.* 2010, **53,** 3088–3093.
2. Q. Zhou, P. Dong, L. Liu, B. Cheng, *Colloids Surf. A Physicochem. Eng. Asp.* 2005, **253,** 169–174.
3. W. Stober, A. Fink, E. Bohn, *J. Colloid Interface Sci.* 1968, **26,** 62–69.
4. C. Jing, Y. Zhang, J. Zheng, S. Ge, J. Lin, D. Pan, N. Naik, Z. Guo, *Particuology* 2022, **69,** 111–122.
5. S. Y. Lim, C. S. Law, L. Liu, M. Markovic, A. D. Abell, A. Santos, *Catal. Sci. Technol.* 2019, **9,** 3158–3176.
6. W. S. A. El-Yazeed, A. I. Ahmed, *Inorg. Chem. Commun.,* 2019, **105,** 102–111.
7. X. Li, Y. Wu, Y. Shen, Y. Sun, Y. Yang, A. A. Xie, *Appl. Surf. Sci.* 2018, **427,** 739–744.
8. P. Birnal, M. C. Marco de Lucas, I. Pochard, F. Herbst, O. Heintz, L. Saviot, B. Domenichini, L. Imhoff, *Appl. Surf. Sci.* 2023, **609,** 155213.
9. P. Birnal, M. C. Marco de Lucas, I. Pochard, B. Domenichini, L. Imhoff, *Appl. Surf. Sci.* 2020, **512,** 145693.
10. Z. Zhao, H. He, Y. Zhu, X. Wang, Y. Shen, A. Xie, *J. Alloys Compd.* 2021, **858,** 158356.